Chapter 3

THE LARGE HADRON COLLIDER AND THE ATLAS DETECTOR

This chapter provides a brief introduction to the world's largest and most powerful particle accelerator, the Large Hadron Collider (LHC). I will describe the LHC in the context of this thesis and how the ATLAS detector fits into the picture. More information about the design, contruction, and operation of the LHC can be found in [1].

The rest of the chapter is organized as follows: section 3.1 describes the LHC and the experiments located along the collider; section 3.3 describes the operating schedule of the LHC; and sections 3.4 to 3.8 describes the ATLAS detector instrumentation used in this thesis whose successful operation provided the datasets that allowed me to perform my analysis.

3.1 Overview

The Large Hadron Collider (LHC) [1] at the European Organization for Nuclear Research (European Organization for Nuclear Research (CERN)) is a 27 km super-conducting particle accelerator located approximately 100 m underground. A diagram of the LHC is shown in fig. 3.1.

The LHC's role is to collide beams of protons in opposite directions at four locations along the ring of the machine. Each of these four locations contains an excavated cavern that houses one of the four LHC experiments: ATLAS [3], CMS [4], LHCb [5], and ALICE [6]. The beams of protons are guided around the accelerator ring using 1232, 15 m long super-conducting dipole magnets [7] which provide a strong 8.3 T magnetic field for bending the

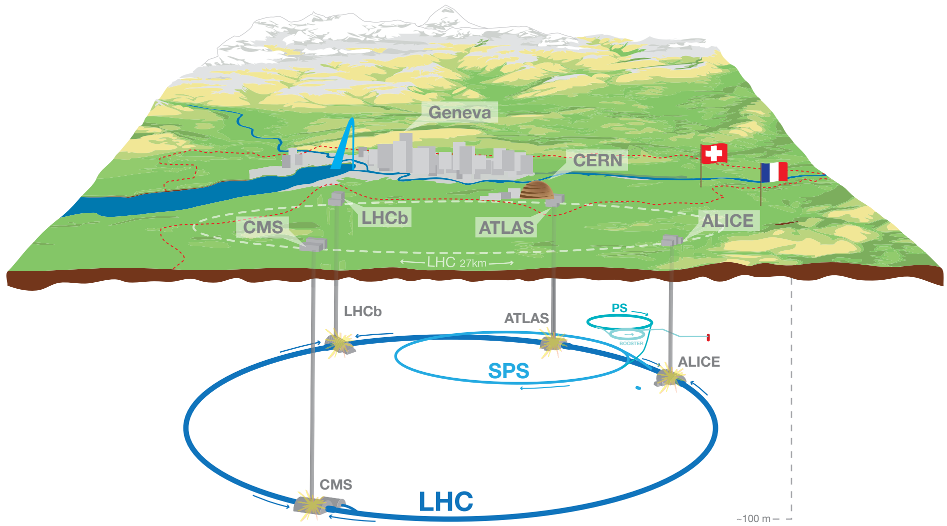

Figure 3.1: [2] A diagram of the LHC which sits on the border between Switzerland and France, near the city of Geneva. There are four main experiments located here: ALICE, ATLAS, CMS, and LHCb. All of the experimental apparatus are located around 100 m underground where the stable rock is located. Also shown here is the Super Proton Synchotron which is the second-to-last stage of the injector chain before the particles enter the LHC tunnel.

proton trajectories. 392 main quadrupole magnets [7], each 5–7 m long, are used to help keep the proton bunches in a tight beam with four magnetic poles arranged symmetrically around the beam pipe to squeeze the beam either horizontally or vertically. The aim of the LHC is to reveal the physics beyond the Standard Model with center-of-mass collision[1] energies of up to $\sqrt{s} = 14\,\text{TeV}$.

However, it should be noted that the LHC is only the last step in the injector chain, where

[1]Technically, it's bunches of protons colliding with bunches of protons, rather than a single proton with a single proton; each proton has $\sqrt{s}/2$ energy.

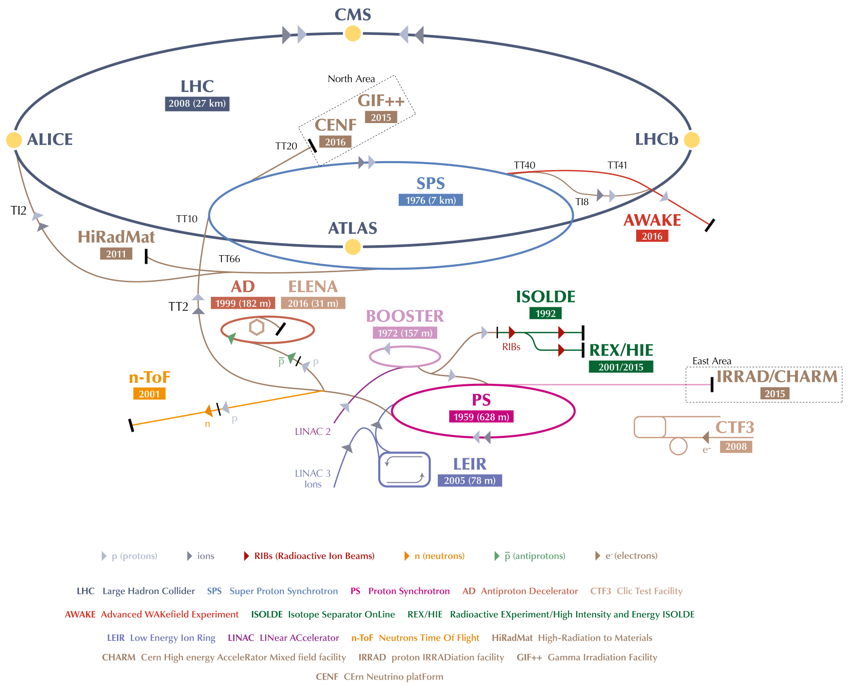

Figure 3.2: A diagram of LHC injector complex [1, 8]. Protons are accelerated in the following chain: Linac2→Proton Synchotron Booster→Proton Synchotron→Super Proton Synchotron→Large Hadron Collider.

protons are accelerated from low energies in defined steps to their final energy as illustrated in fig. 3.2. Their journey starts at a linear accelerator aptly called Linac2[2] which accelerated protons to 50 MeV. The protons are injected in to the Proton Synchotron Booster (PSB), which accelerates them to 1.4 GeV. After the PSB, the protons are sent to the Proton Synchotron (PS) to reach 25 GeV of energy. They are then sent to the Super Proton Synchotron (SPS) where the protons are accelerated up to 450 GeV of energy. Finally, they are injected into the LHC. Under nominal operating conditions, where the LHC can run for many hours[3], each proton beam can have 2808 bunches and on the order of 10^{11} protons per bunch.

[2] Linac1 was retired in early 1990s.

[3] Current record in 2015-2016 data run was 37 h with fill #5045.

3.2 LHC Upgrades

After 2019, the statistical gain in running the accelerator without a considerable luminosity increase beyond its design value will become marginal. The running time at a constant luminosity and $\sqrt{s}$ necessary to half the statistical error in the measurements will be more than ten years at the end of 2019. Therefore to maintain scientific progress and to explore its full capacity, the LHC will need to have a decisive increase of its luminosity. The CERN Council has updated the LHC upgrade plan taking this into consideration. The schedule for the upgrades and operation of the LHC accelerator complex, leading to the High Luminosity LHC (HL-LHC) [9], is illustrated in Fig. 3.3.

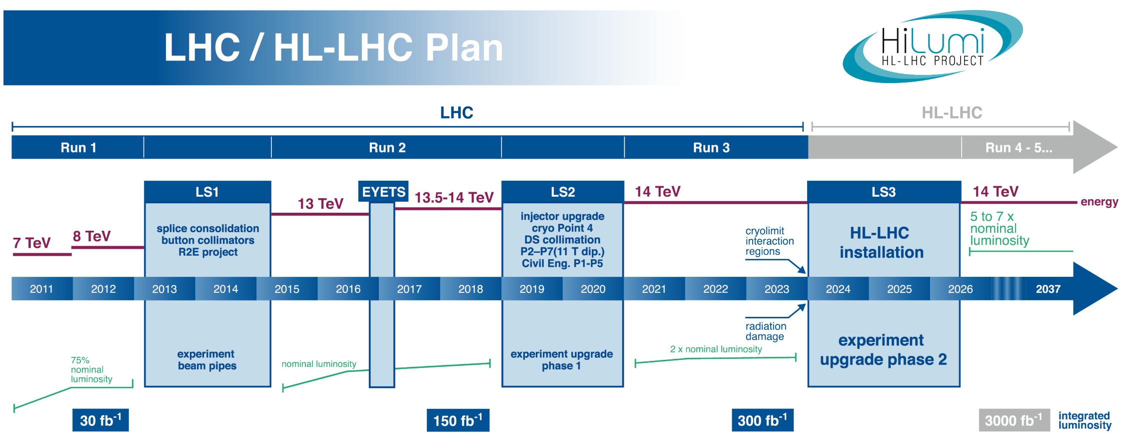

Figure 3.3: LHC and High Luminosity LHC plan [9].

3.3 Operation of the LHC in Run 2

The last thing I want to cover in discussing the LHC is about the data it provides from a physics point of view. The center-of-mass energy and integrated luminosity are two of the most important characteristics of the dataset. For the 2015-2016 data-taking run which this thesis is written on, the center-of-mass energy is $\sqrt{s} = 13\,\text{TeV}$ with a total integrated luminosity of 36.1 fb^{-1} as seen in fig. 3.4. The LHC will be shut down in 2018-2012 for a series of repairs and upgrades, after which it is expected to be run at $\sqrt{s} = 14$ TeV.

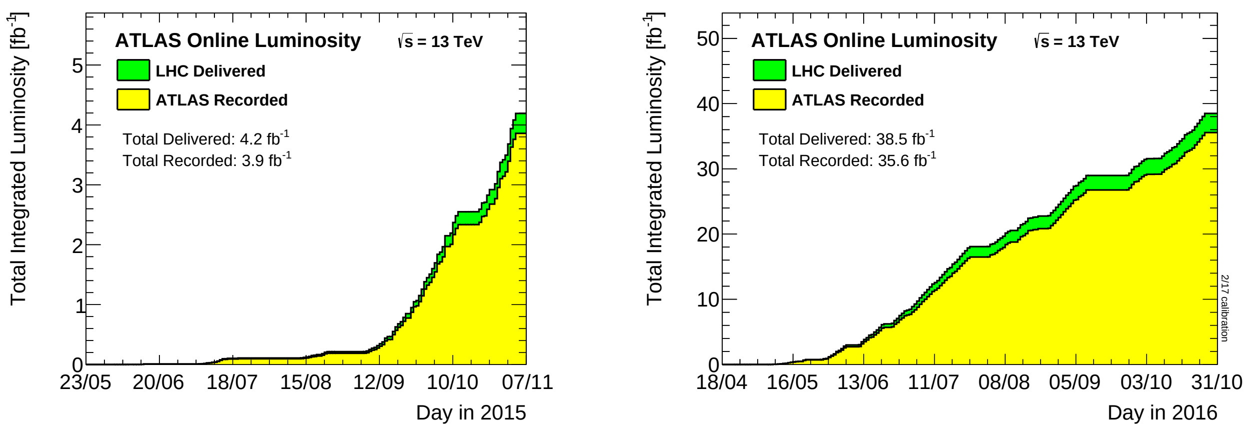

(a) 2015 (b) 2016

Figure 3.4: [10] Cumulative luminosity versus time delivered to (green) and recorded by ATLAS (yellow) during stable beams for proton-proton collisions at $\sqrt{s} = 13$ TeV center-of-mass energy in (a) 2015 and (b) 2016. The difference between delivered and recorded luminosity reflects the small inefficiency of the data acquisition in ATLAS. The uncertainty in the combined 2015+2016 integrated luminosity is 2.1%. It is derived, following a methodology similar to that detailed in [11], from a calibration of the luminosity scale using x-y beam-separation scans performed in August 2015 and May 2016.

Luminosity can be a little be confusing to understand as physicists often have two different, related terms. The integrated luminosity in fig. 3.4 is proportional to the total number of collisions (or events) recorded while the instantaneous luminosity in fig. 3.5 is proportional to the bunch crossing rate and represents the potential number of collisions per second. The integrated luminosity, L_{int} is then meant to be understood as the integral of the instantaneous luminosity $L_{\text{inst.}} \equiv L$[4] over the data collection period. That is,

$$L_{\text{int}} = \int L \mathrm{d}t = 36.1\,\mathrm{fb}^{-1} \tag{3.1}$$

and the machine luminosity depends only on the beam characteristics [1]. For a Gaussian

[4]This is often referred to as the machine luminosity as well, or just L.

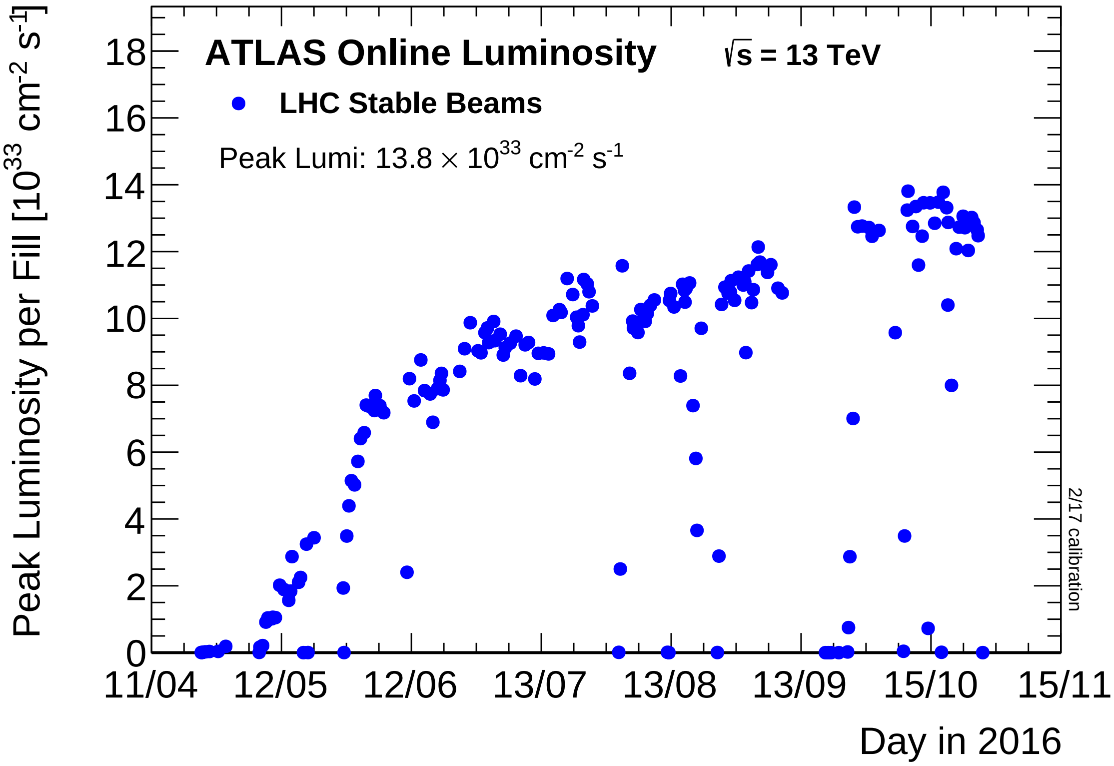

Figure 3.5: [10] The peak instantaneous luminosity delivered to ATLAS during stable beams for proton-proton collisions at $\sqrt{s} = 13\,\text{TeV}$ center-of-mass energy is shown for each LHC fill as a function of time in 2016. The luminosity is determined using counting rates measured by the luminosity detectors.

beam, this can be written as

$$L = \frac{N_b^2 n_b f_{\text{rev}} \gamma_r}{4\pi \varepsilon_n \beta^*} F, \tag{3.2}$$

where N_b is the number of particles per bunch[5], n_b is the number of bunches per beam, f_{rev} is the revolution frequency, γ_r is the relativistic gamma factor, ε_n is the normalized transverse beam emittance, β^* is the beta function[6] at the collision point, F is the geometric luminosity

[5] Assuming that each beam has the same number of bunches N_b.

[6] Small β^* corresponds to a narrower beam, related to the transverse size of the particle beam at the interaction point. The narrower the beam, the more "squeezed" it is, and so this also corresponds to a smaller geometric factor, F.

reduction factor due to the crossing angle at the interaction point:

$$F = \left(1 + \left(\frac{\theta_c \sigma_z}{2\sigma^*}\right)^2\right)^{-1/2}, \tag{3.3}$$

where θ_c is the full crossing angle at the interaction point, σ_z is the RMS bunch length, and σ^* is the transverse RMS beam size at the interaction point. Using the nominal LHC parameters in [1] and summarized in table 3.1, the expected peak luminosity is $L = 1\mathrm{e}34\,\mathrm{cm}^2\,\mathrm{s}^{-1} = 0.36\,\mathrm{fb}^{-1}/\mathrm{h}$ for both ATLAS and CMS, which are the high-luminosity experiments at the LHC. A classical route to increase the luminosity is to reduce the β^* with stronger and larger aperture quadrupole magnets. This requires a larger crossing angle which reduces the geometrical factor, but is compensated for with crab cavities to generate transverse electric fields [12].

The larger the integrated luminosity, the larger the data set which enables the study of physics beyond the Standard Model and precision measurements of rare processes.

3.3.1 Pile-up at the LHC

Due to the cross-section for interaction and the total number of protons per bunch, the probability to observe multiple proton-proton interactions per bunch crossing increases as the luminosity increases. The multiple proton-proton interactions is referred to as **pile-up** but comes in two main forms:

1. **in-time** pile-up refers to the multiple proton-proton interactions that in the same bunch crossing that is currently being recorded, and
2. **out-of-time** pile-up refers to the effect of seeing multiple proton-proton interactions outside of the bunch crossing that is currently being reecorded.

Parameter	Run 2 LHC [1]
Circumference	26659 m
Beam energy in collision	7 TeV
Protons per bunch N_b	1.15e11
Bunches per beam n_b	2808
Radiofrequency Cavity frequency	400 MHz
Proton speed β	0.9999999991
Lorentz factor γ_r	7460.523
Revolution frequency f_{rev}	11.2455 kHz
Beam current	0.58 A
Crossing angle θ_c	285 µrad
Beta function at collision point β^*	0.55 m
Transverse beam emittance ε_n	3.75 µm
RMS bunch length σ_z	7.55×10^{-2}m
Transverse RMS beam size σ^*	16.6 µm
Expected peak luminosity	$10\,\text{nb}^{-1}/\text{s}$

Table 3.1: A summary of the LHC typical parameters for Run 2 operating and data taking as taken from [1]. This design is based on the 25 ns bunch crossing separation. At full power, the LHC beam intensity is given above. Other parameters, such as beam amplitude parameters are typical values which are kept small to achieve high luminosity.

Out-of-time pile-up is primarily an electronic effect due to the long integration times of various detector components. The 2015-2016 data run had up to 50 proton-proton interactions per bunch crossing as seen in fig. 3.6. Pile-up is often refered to as μ, and the time-average pile-up is reported as $\langle\mu\rangle$. The actual number of interactions per bunch-crossing can fluctuate with Poisson statistics. The wide variation seen in the figure is due to two primary effects. During a run of proton-proton collisions, the number of protons in a bunch will decrease over time (as does luminosity) and so μ will also decrease. The peak μ is often seen at the start of a run, with the peak luminosity. The other main source of the fluctuation is due to the tweaking of the LHC beams, such as changing β^* to get a narrower or wider beam. These sorts of large-scale changes to the beam properties are often either due to optimizing the beam for maximum physics impact or to respond to issues with subsystems of the accelerator complex such as power issues or magnet issues.

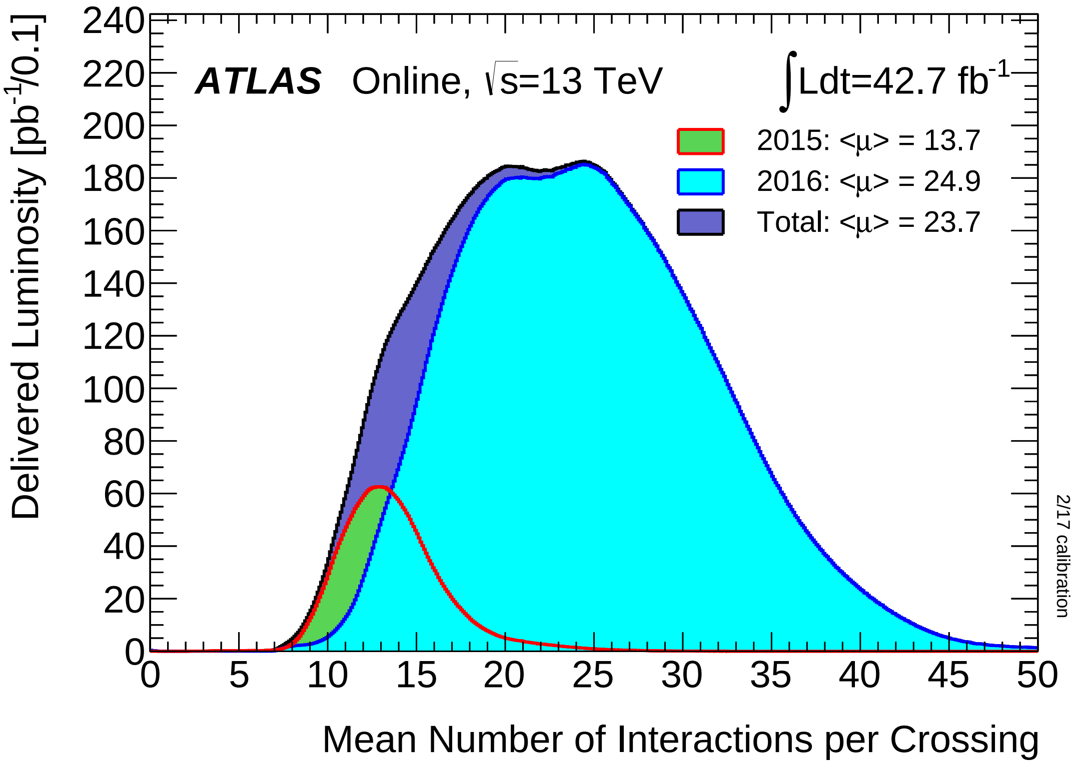

Figure 3.6: [10] The distribution of the mean number of interactions per crossing for the 2015-2016 proton-proton collision data at $\sqrt{s} = 13\,\text{TeV}$ center-of-mass energy. All data delivered to ATLAS during stable beams is shown, but not necessarily all of this data is suitable for an analysis.

Pile-up is very important for future upgrades as the LHC will have an increased luminosity. Further studies of pile-up in the context of the instrumentation upgrades I work on are described in ??.

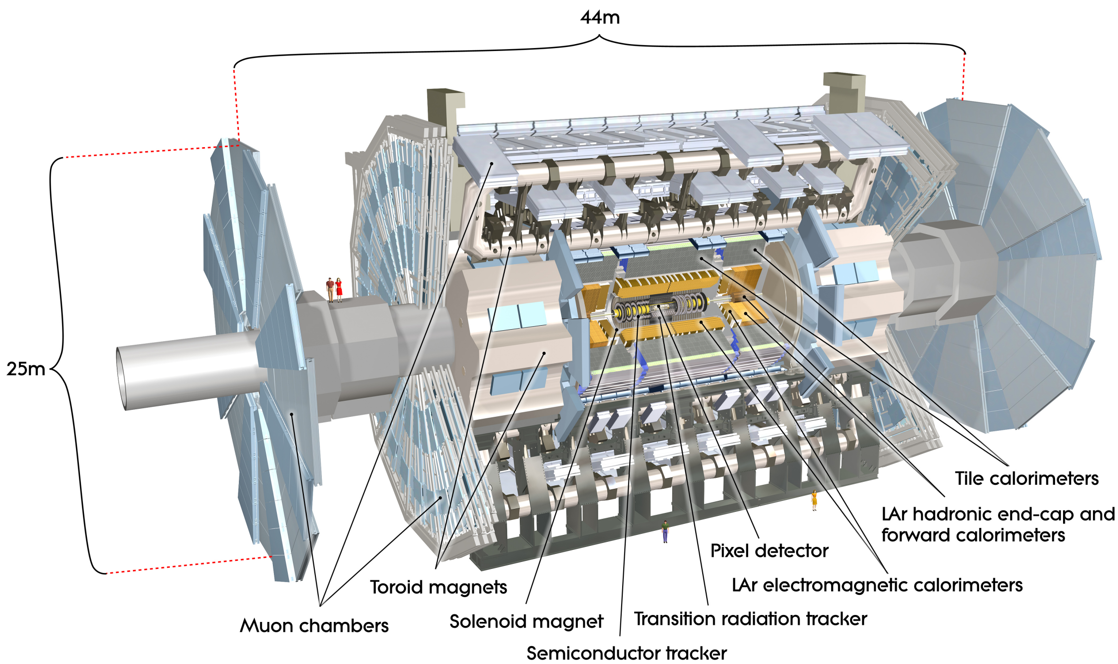

Figure 3.7: [3] A cut-away view of the ATLAS detector. The dimensions of the detector are 25 m in height and 44 m in length. The overall weight of the detector is approximately 7000 t. This figure groups up major instrumentation components of the detector. Two people in red are shown for scale just to the right of the muon chambers on the left side of the figure.

3.4 ATLAS Overview

The ATLAS detector fig. 3.7 is one of four main experiments at the LHC and is centered at Point 1, a collision point of the LHC. With over 100 million electronic channels and over 3000 km of cabling, it is one of the largest and most complex particle detectors in existence today. The detector is located approximately 100 m underground and centered around the LHC beam pipe. See section 3.5 for details about the geometry of the detector with respect to LHC. Particles produced at the interation point at the center of the detector spread out in all directions, hence the encompassing cylindrical design of the ATLAS detector. The ATLAS detector is built up of 3 main sub-detector pieces: tracking system, calorimetry, and muon tracking system.

The rest of the sections are ordered as seen in fig. 3.7 from the inside-out, providing an overview of each sub-detector and its role in studying high energy particle physics collisions. Section 3.6 discusses the Inner Detector (ID), a tracking system that uses ionization to measure the trajectory of charged particles with help of the enclosing 2 T solenoid magnet. Section 3.7 describes the calorimetry system surrounding the solenoid magnet, composed of the electromagnetic and hadronic calorimeters that use scintillation and ionization to measure the energy of electrons, photons, and hadrons. The muon system, described in section 3.8, surrounds the calorimeters and contains toroid magnets that uses ionization to measure the trajectories of deflected muons leaving the detector. Neutrinos are the only other standard model particles that leave the detector, but undetected. This is neatly depicted in fig. 3.8 which shows a cartoon diagram of a slice of the detector with the various particle interactions.

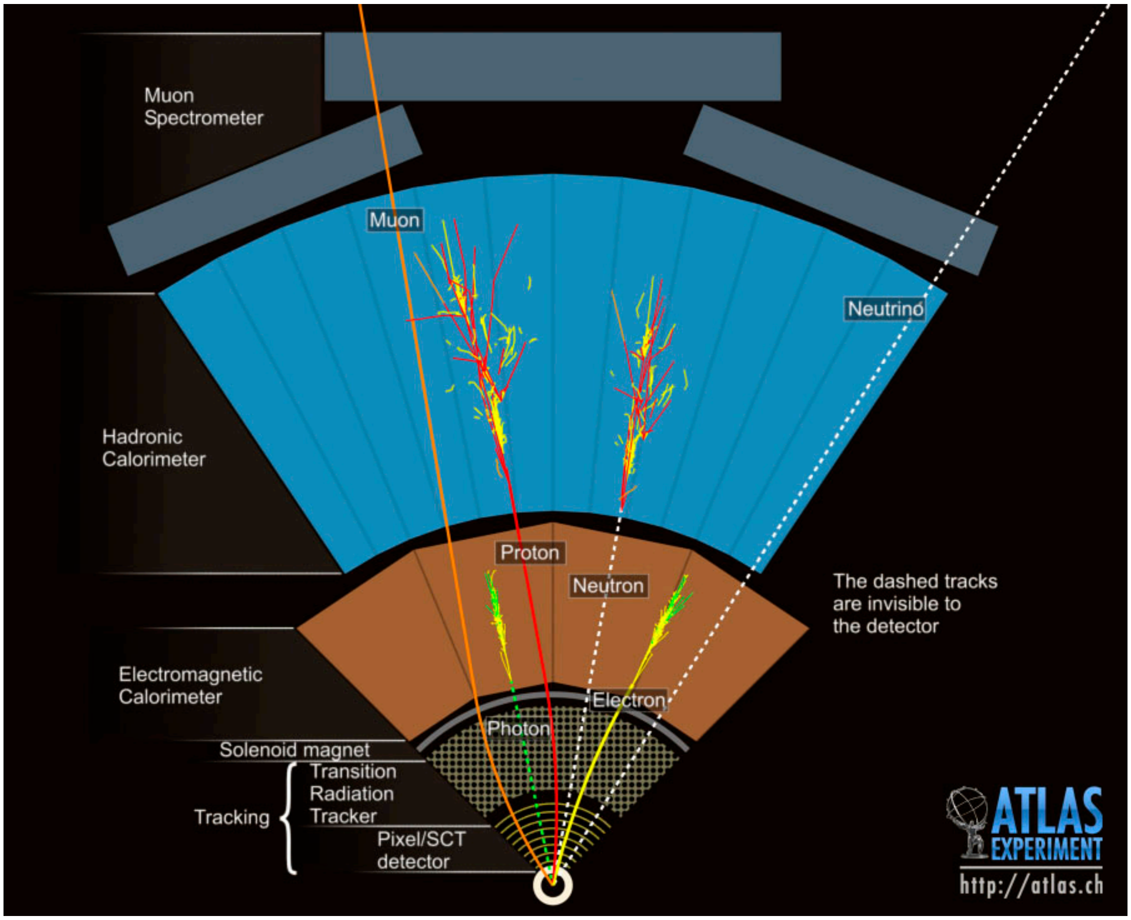

Figure 3.8: [3] A slice of the ATLAS detector depicting the various particle interactions with each component of the detector. Dashed tracks in this figure are invisible to the detector component that the line is overlaid on top of. Muon track (orange) and neutrinos (dashed, white) pass through the entire detector. Electrons (yellow/green), photons (yellow/green), and hadrons (red/yellow) are fully absorbed by the calorimeter system. Charged particles like protons, electrons, and muons are curved by the solenoid magnet within the tracking system.

3.5 ATLAS Geometry

ATLAS uses a right-handed coordinate system with its origin at the nominal interaction point in the center of the detector. The positive x-axis is defined by the direction from the interaction point to the center of the LHC ring, with the positive y-axis pointing upwards, while the beam direction defines the z-axis as seen in fig. 3.9. The x-y plane is perpendicular to the beam line and is referred to as the transverse plane. Cylindrical coordinates (r, ϕ) are used in the transverse plane, ϕ being the azimuthal angle around the z-axis. The objects measured in the ATLAS detector have momenta that can be described using two quantities $\vec{p} = (p_{\mathrm{T}}, p_z)$ with p_{T} the momentum of the particle in the transverse plane and p_z the momentum of the particle along the beam axis.

The pseudorapidity η in fig. 3.10 is defined in terms of the polar angle θ by

$$\eta = -\ln\tan\left(\frac{\theta}{2}\right). \tag{3.4}$$

where $\eta = 0$ is perpendicular to the beam axis and large values of $|\eta|$ are close to the beam axis. Positive η is in the positive z-side and negative η is on the negative z-side.

Rapidity y is defined as

$$y = \frac{1}{2}\ln\left[\frac{E + p_z}{E - p_z}\right], \tag{3.5}$$

where E denotes the energy and p_z is the component of the momentum along the beam direction. The position of an object is often described in terms of (η, ϕ). The distance ΔR between objects in η-ϕ space is

$$\Delta R = \sqrt{(\Delta\eta)^2 + (\Delta\phi)^2} \tag{3.6}$$

The choice of geometry for pseudorapidity (or rapidity) and ϕ is because differences in

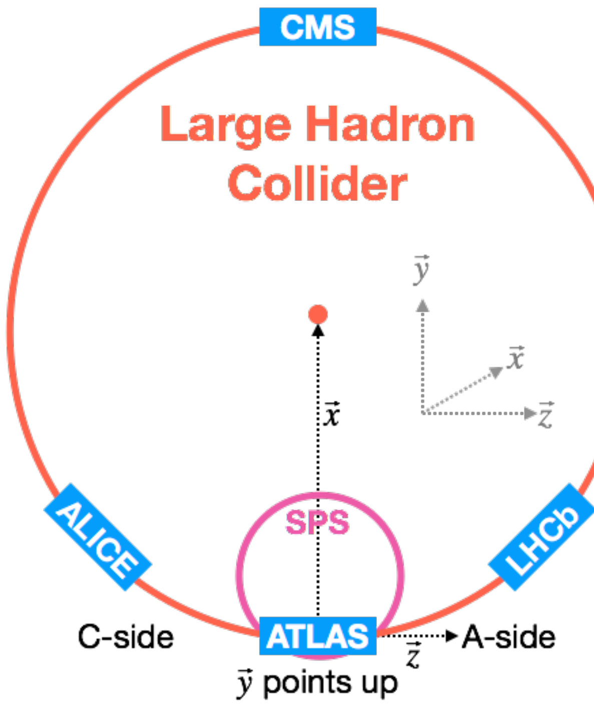

Figure 3.9: A top-down cartoon of the LHC, the SPS, and the four experiments at the LHC: ATLAS, CMS, LHCb, and ALICE. A common coordinate system is used in ATLAS. The positive x-axis points from the interaction point at the center of the ATLAS detector to the center of the LHC ring. the positive y-axis points from the interaction point upward to the surface of the earth. The z-axis runs along the beam line, with the detector half at positive z-values referred to as the "A-side" (Geneva side) and the detector half at negative z-values referred to as the "C-side" (Jura side).

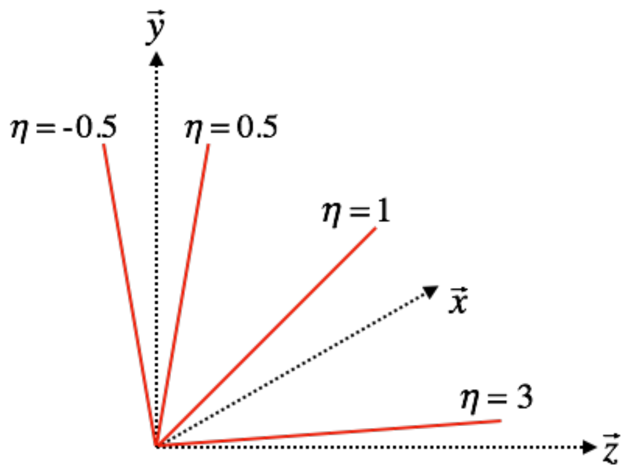

Figure 3.10: A cartoon representation of selected pseudorapidity (η) values overlaid on cartesian geometry axes (dashed black lines). Red lines are drawn for $\eta = \pm 0.5, 1.0, 3.0$.

rapidity are Lorentz invariant under boosts along the beam axis. If you boost eq. (3.5) along the z-axis

$$\begin{aligned} y' &= \frac{1}{2}\ln\left[\frac{\gamma E - \beta\gamma p_z + \gamma p_z - \beta\gamma E}{\gamma E - \beta\gamma p_z - \gamma p_z + \beta\gamma E}\right] \\ &= y + \frac{1}{2}\ln\left[\frac{1-\beta}{1+\beta}\right] \\ &= y + \tanh^{-1}\beta. \end{aligned} \tag{3.7}$$

So the difference in rapidities is Lorentz-invariant. Since $\Delta\phi$ is measured in the x-y plane, it is also invariant under Lorentz boosts along the beam axis. This means that ΔR is also Lorentz-invariant.

3.6 Tracking in the Inner Detector

The inner detector [13, 14] is the first part of ATLAS to see the outgoing particles of the proton-proton collisions. It is built around the beam pipe with cylindrical geometry as

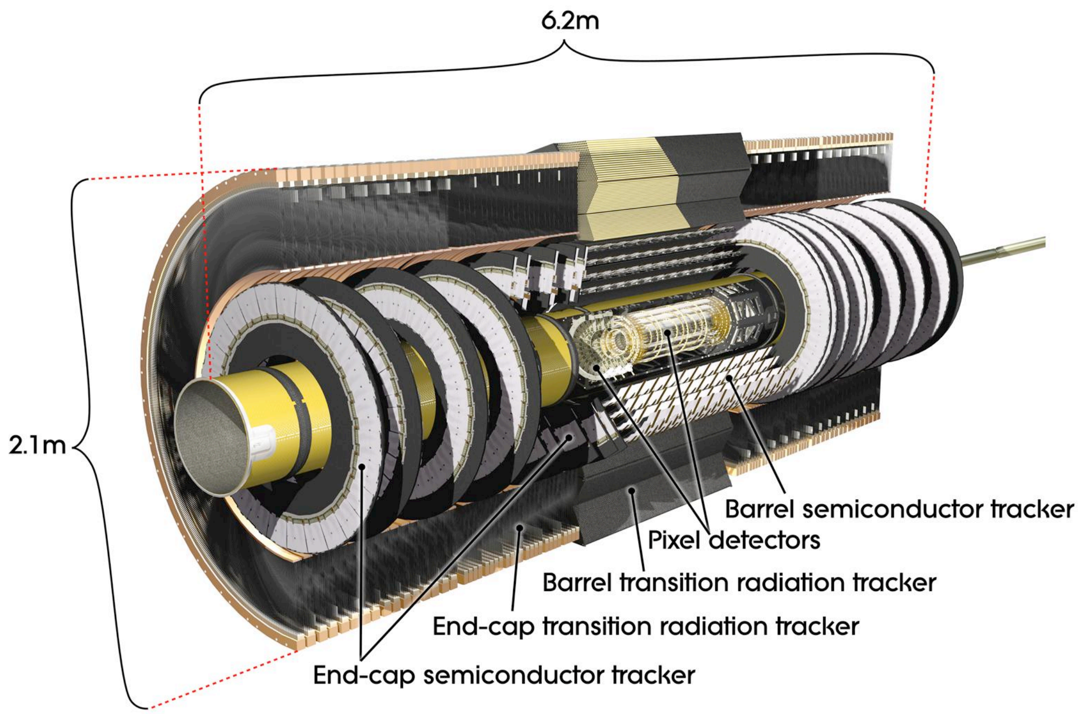

Figure 3.11: [3] A longitudinal view of the ID compromising of the three main pieces: pixel detector, semiconductor tracker, and transition radiation tracker. It is 6.2 m in length and 2.1 m in height.

shown in fig. 3.11 within a 2 T solenoid magnet. It is designed to be compact with excellent momentum resolution of charged particle tracks above $p_{\mathrm{T}} \geq 500\,\mathrm{MeV}$[7] for $|\eta| < 2.5$. The inner detector is made of three specific sub-components as seen in fig. 3.13.

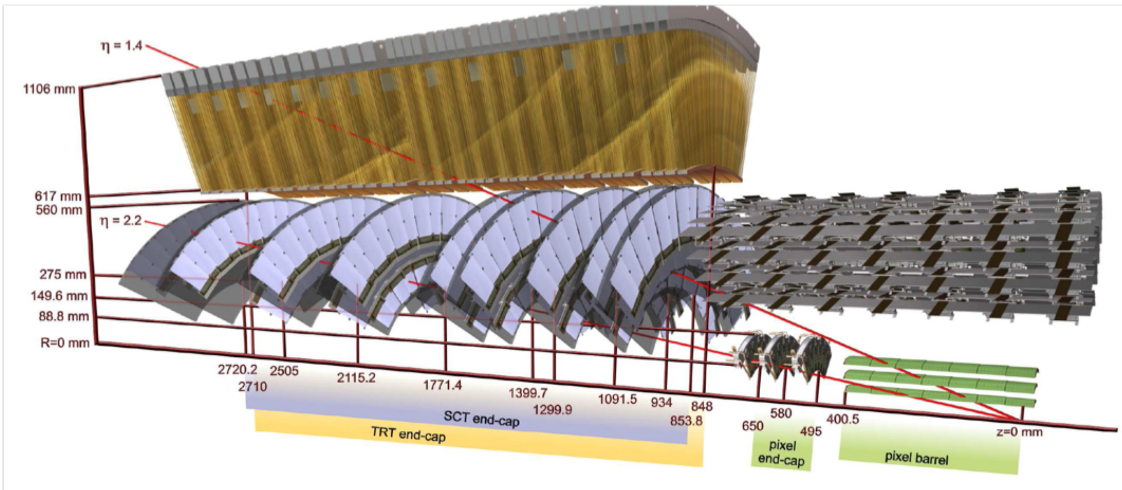

Figure 3.12: [3] Drawing showing the sensors and structural elements traversed by two charged tracks of $p_{\mathrm{T}} = 10\,\mathrm{GeV}$ in the end-cap ID at $\eta = 1.4$ and $\eta = 2.2$. The track at $\eta = 1.4$ passes through the beam pipe, the three pixel layers, four Semiconductor Tracker (SCT) disks with double layers, and approximately 40 straws Transition Radiation Tracker (TRT) end-cap. A particle at $\eta = 2.2$ passes through the beam, only the first pixel layer, two of the end-cap pixel disks, and the last four end-cap SCT disks, but does not pass through the TRT straws which covers $|\eta| \leq 2.0$.

The pixel detector [15] is the closest to the beam pipe and has 80 million pixels (or readout channels) covering $1.7\,\mathrm{m}^2$ for $|\eta| \leq 2.5$. Each pixel has an area[8] of $20000\,\mu\mathrm{m}^2$ with a position resolution of[9] $14\,\mu\mathrm{m}$ in ϕ and $115\,\mu\mathrm{m}$ in z directions[10]. The three barrel layers have 1456 pixel modules, each with 46080 readout channels. The three pixel disks in each endcap have

[7] The solenoid magnetic field strength of 2 T means that charged particles need $p_{\mathrm{T}} \geq 500\,\mathrm{MeV}$ at 2 T to escape the ID and reach the calorimeters. The magnetic field from the solenoid is not perfect and fluctuates down to 0.5 T on the ends of the detector. A minimum p_{T} threshold is applied to reduce the rate of fake tracks.

[8] $50\,\mu\mathrm{m}$ in ϕ direction and $400\,\mu\mathrm{m}$ in z direction, along beam axis.

[9] area$/\sqrt{12}$ is the upper limit in resolution for a digital readout [16]. Modern pixel detectors can achieve better resolution by using charge measurement to determine which pixel a charged particle was closer to.

[10] Better resolution in the ϕ direction as the this is enclosed in a solenoid magnet so that charged particles will bend along the ϕ direction.

144 modules, 6.6 million readout channels. The pixel detector provides one measurement per barrel layer for each charged particle track and full pattern recognition capability to reconstruct tracks at nominal LHC parameters. It is also crucial to the identification and reconstruction of both primary and secondary vertices; the latter which is seen in the decay of particles containing a b-quark or for b-tagging of jets, necessary to perform the analysis search in **??**. This is highlighted in green in fig. 3.13.

The semiconductor tracker [17] surrounds the pixel detectors. This is a silicon microstrip tracker that consists of 4088 two-sided modules with over 6 million strips (or readout channels) covering $63\,\mathrm{m}^2$ for $|\eta| \leq 2.5$. All of the modules are distributed over four barrel layers and 9 disks in each endcap (18 endcap disks total). The readout strips are placed $80\,\mu\mathrm{m}$ and rotated by 50 mrad with respect to each other, provide a position resolution of $17\,\mu\mathrm{m}$ in the transverse plane and $580\,\mu\mathrm{m}$ in the z-axis. The SCT is designed to provide between 4 and 9 precision measurements per track in the intermediate radial range. This component, along with the pixel detector, contributes to the measurement of momentum, impact parameter, and vertex identification of a charged particle track. This is highlighted in blue in fig. 3.13.

The last component of the ID is the transition radiation tracker [18, 19]. The TRT is made of over 350,000 drift tubes (straw tubess, or readout channels) covering $12\,\mathrm{m}^3$ of volume for $|\eta| < 2.0$. The basic detector element, straws, are 4 mm in diameter, 144 cm (37 cm) long in the barrel (endcap) providing a position resolution of $130\,\mu\mathrm{m}$ [20][11] in ϕ. In the barrel (endcap), there are 52544 (245760) straws over 73 layers (160 straw planes) which provide transition radiation[12] tracking for charged particle identification. All the charged particle tracks will traverse through at least 36 straws[13]. The charge collection time in the straw is

[11] This resolution depends strongly on the drift-time (or drift-distance). See studies in Figs. 20-23 from [18]

[12] Transition radiation is a form of radiation when a charged particle passes through the 70%/27%/3% Xenon/Carbon-Dioxide/Oxygen mixture in the straw tubes. The energy of the photon emitted is proportional to the relativistic Lorentz factor.

[13] Only for $|\eta| < 2.0$. The exception is in the region between barrel and end-cap where this number goes

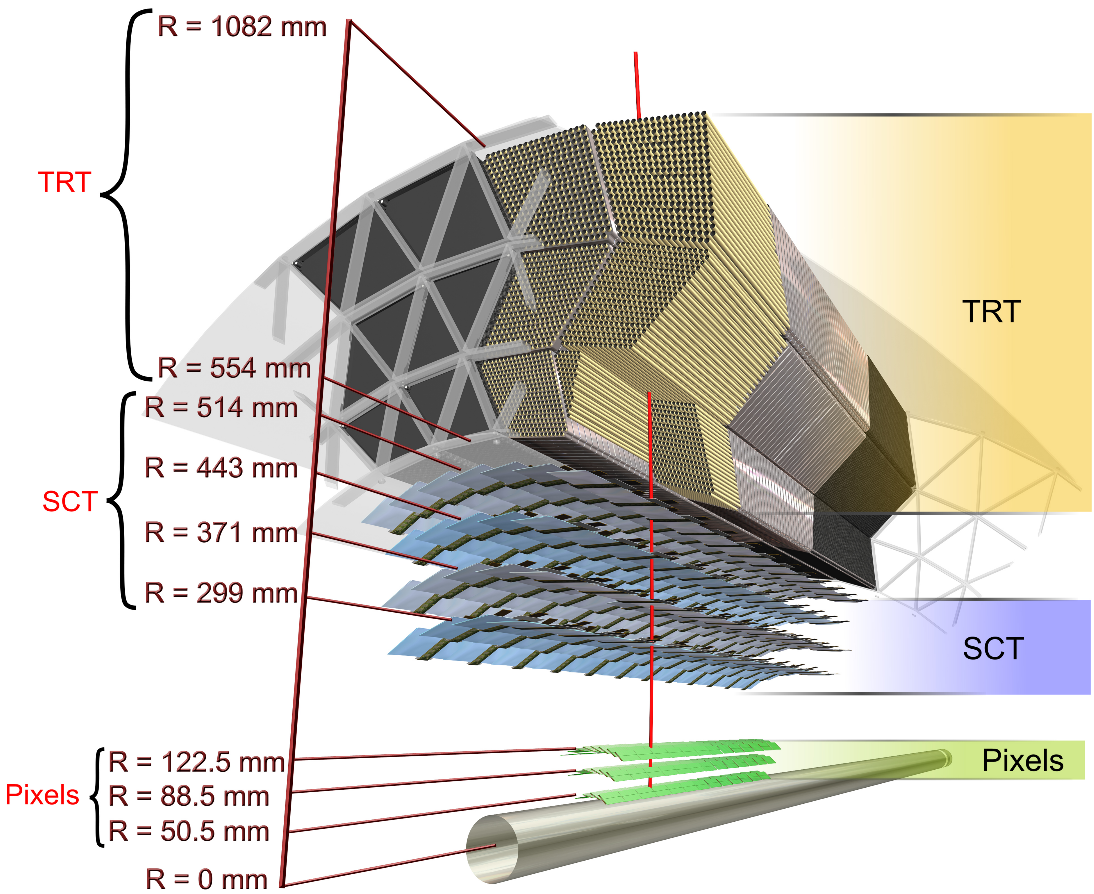

Figure 3.13: [3] A radial view of the ID with the detector elements crossed by a charged particle $p_{\mathrm{T}} = 10\,\mathrm{GeV}$. The track pases through the beam pipe, three pixel layers, four SCT disks with double layers, and approximately TRT 40 straws.

an important parameter for tracking performance. At a fixed transverse momentum for a charged particle, a light-mass charged particle will emit more transition radiation photons than a heavier-mass charged particle[14]. Therfore, the TRT is an important component for discrimination between electrons and charged hadrons for $|\eta| < 2.0$.

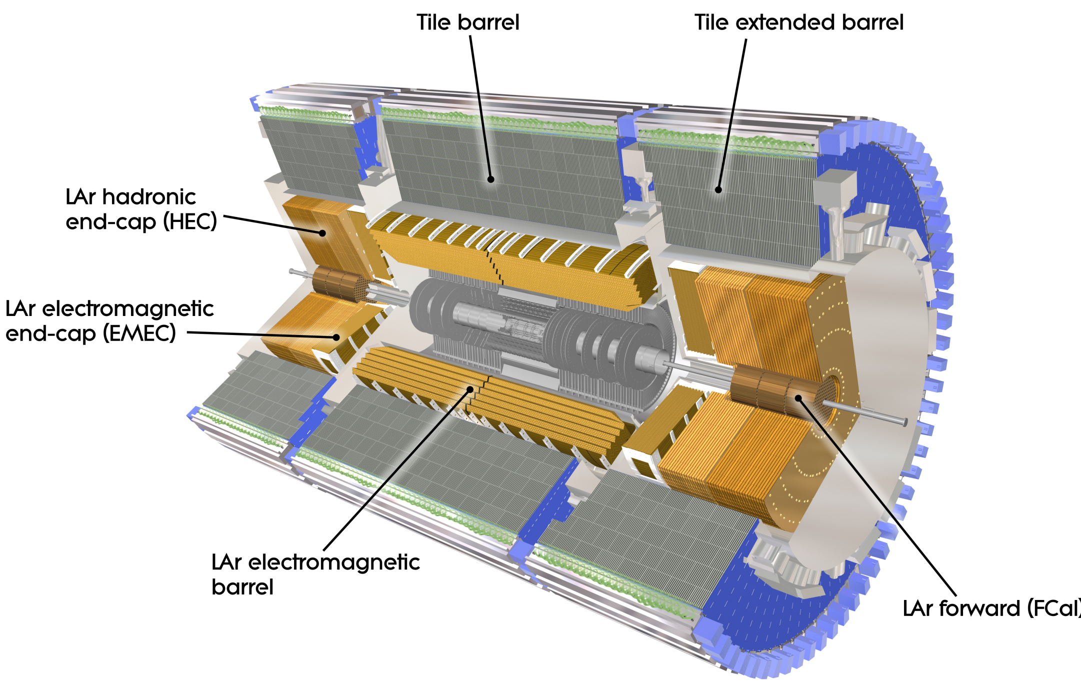

Figure 3.14: [3] A longitudinal, cut-away view of the ATLAS calorimeter system showing: the tile calorimeter barrel, the tile calorimeter extended barrel, the liquid argon electromagnetic barrel, the liquid argon electromagnetic end-cap, the liquid argon hadronic end-cap, and the forward calorimeter.

down to at least 22 straws.

[14]Recall that these charged particles are travelling curved trajectories in the solenoid's magnetic field and heavier particles bend less than lighter particles. Lighter particles spend more time in the drift tubes and thus emit more radiation.

3.7 Calorimetry and the Calorimeter System

An overview of the ATLAS calorimetry system [21, 22] is seen in fig. 3.14. There are two different types of calorimeters used in this system: hadronic and electromagnetic. An electromagnetic calorimeter is designed to measure the energy of particles that interact via the electromagnetic interaction[15], while a hadronic calorimeter is designed to measure particles that interact via the strong nuclear force. ATLAS uses both of these types of calorimeters, as a sampling calorimeter. A sampling calorimeter is one in which the "active" material that provides the detectable signal is different from the dense "absorber" material that reduces particle energy. Because the dense material is chosen to absorb a lot of the particle energy, only a fraction of the energy is measurable by the detector sensors. This requires a calibration to the measured calorimeter energy by studying the calorimeter response, and will be discussed in more detail in **??**. The calorimeters have a large responsibility in providing coverage for the full $-4.9 < \eta < 4.9$ range, while having sufficient granularity for precision measurements, and providing containment for both electromagnetic and hadronic showers from electrons, photons, and hadrons (see fig. 3.8). This containment is important for punch-through, where energy leaks outside the calorimeters to the muon spectrometers, but also to ensure a good $E_{\mathrm{T}}^{\mathrm{miss}}$ measurement, which is crucial for many physics programs, in particular supersymmetry searches like mine (see **??**).

The LAr electromagnetic barrel (EMB) and EMEC are Lead/Liquid-Argon detectors with "accordion geometry" as seen in fig. 3.15 covering $|\eta| < 3.2$ for precision electromagnetic shower measurements. This specialized geometry provides complete and uniform coverage over ϕ without any cracks, while allowing low latency readout of the data. This geometry has three radial layers. The first sampling layer, known as "strips", is finely segmented

[15] such as brehmsstrahlung, pair production

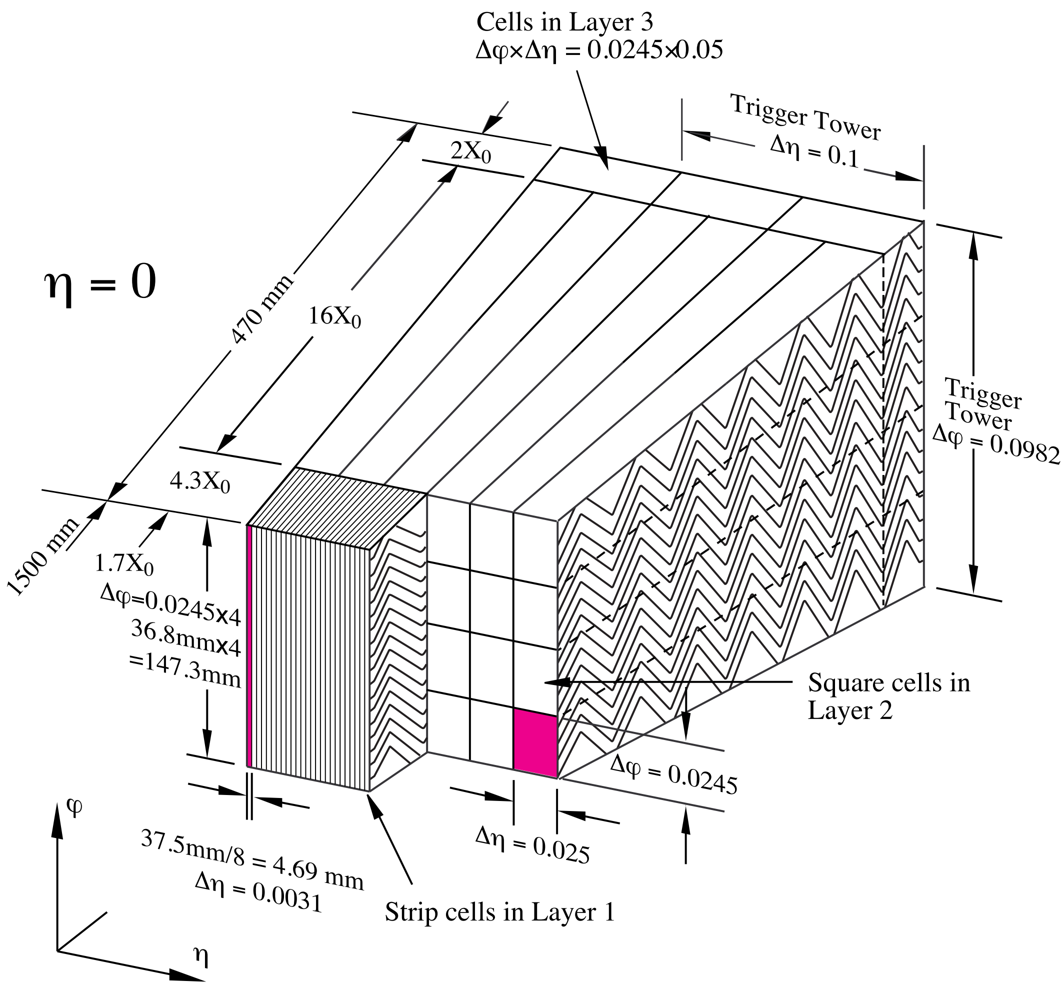

Figure 3.15: [3] This is a sketch of a LAr accordion module where the different layers are visible in ϕ which is pointing up in this figure. The granularity in η and ϕ of the calorimeter cells for each of the three sampling layers and of the trigger towers ($\eta \times \phi = 0.1 \times 0.1$) is also shown. These trigger towers will be discussed more in the **??** section.

in $\Delta\eta = 0.0031$[16] with 8 strips in front of each cell. The second sampling layer, which collects the largest fraction of energy of the electromagnetic shower, has fine segmentation of $\Delta\eta = 0.025$ and $\Delta\phi = 0.0245$. The last layer collects the tail end of the electromagnetic shower, and thus can have a coarser segmentation of $\Delta\eta = 0.05$. The fine "strips" in the first layer allow for discrimination of electromagnetic showers from electrons/photons versus energetic pions. For example, a neutral pion can shower to photons ($\pi^0 \to \gamma\gamma$) and the angular distance between the two photons can be small[17], the fine "strips" allow for discrimination of photon showers from pion showers. The EMB is composed of two half-barrels and covers $|\eta| < 1.475$. The LAr EMEC is composed of two wheels and covers the region $1.375 < |\eta| 3.2$. An additional thin LAr presampler covering $|\eta| < 1.8$ allows corrections for energy losses upstream of the electromagnetic calorimeter (EMCal).

To measure the energy of hadrons, the hadronic calorimeters Tile, HEC, and forward calorimeter (FCal) cover $0 < |\eta| < 4.9$. The tile calorimeter is a sampling calorimeter using steel as the absorber and scintillator as the active medium covering the region $|\eta| < 1.7$. As seen in fig. 3.14, it is located behind the EMB and EMEC and divided into a long (central) barrel that is 5.8 m in length covering $|\eta| < 1.0$ and two extended barrels on each side of the detector each 2.6 m in length covering $0.8 < |\eta| < 1.7$ with radius $r = 2.28$–4.25 m. Each barrel consists of 64 modules (or wedges) as seen in fig. 3.16. The HEC uses LAr with a Copper/Liquid-Argon sampling calorimeter which covers $1.5 < |\eta| < 3.2$. There are two wheels on each side of the detector, with each wheel consisting of 32 wedge-shaped modules. Finally, the FCal extends the hadronic calorimeter sampling range by providing coverage over $3.1 < |\eta| < 4.9$, with much coarser granularity. There are 3 modules on each side for the FCal, one electromagnetic module (Copper/Liquid-Argon) and two hadronic modules

[16] We would like to resolve two photons coming from the Higgs decay, versus other decays such as a pion.

[17] See [23], a π^0 with $E \sim 50$ GeV will have two decay photons with $\Delta R < 1$ cm at 150 cm from the interaction point. If no sufficient resolution, this looks like a single photon which can also be faked by hadronic showers. For a large background like multijet which has a cross-section of 10e8 larger than $H \to \gamma\gamma$ cross-section, rejecting jets faking photons like these is important for physics impact.

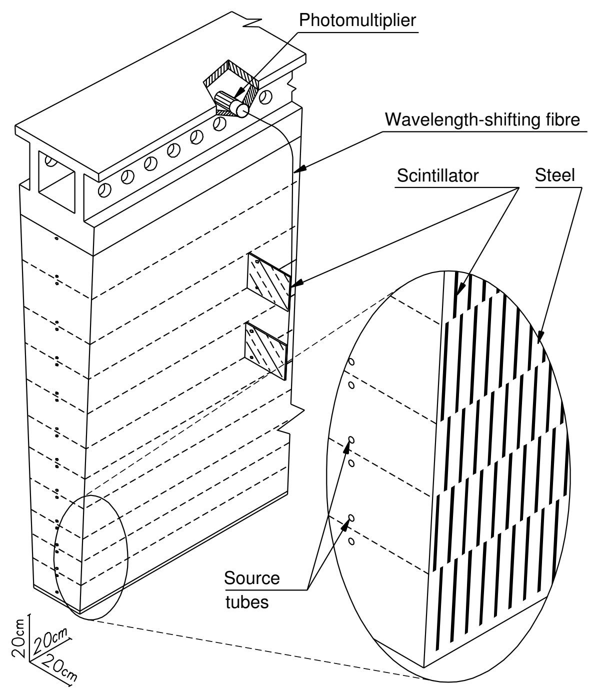

Figure 3.16: [3] This is a sketch of a Tile calorimeter (Tile) module showing how the mechanical assempty and the optical readout are integrated together. The various components of the optical readout are shown: the tiles, the fibers, and the photomultiplier tubes. Each wedge is approximately $\Delta\phi = 0.1$ which is around 20 cm.

(Tungsten/Liquid-Argon).

		Layers			Number of
Detector	Shower	Absorber	Active	Coverage	Channels
EMB	EM	Lead	Liquid-Argon	$\lvert\eta\rvert < 1.475$	99712
EMEC	EM	Lead	Liquid-Argon	$1.375 < \lvert\eta\rvert < 3.2$	62208
Tile	Had	Steel	Scintillator	$\lvert\eta\rvert < 1.0$	5760
	Had	Steel	Scintillator	$0.8 < \lvert\eta\rvert < 1.7$	4092
HEC	Had	Copper	Liquid-Argon	$1.5 < \lvert\eta\rvert < 3.2$	5632
FCal	EM	Copper	Liquid-Argon	$3.2 < \lvert\eta\rvert < 4.9$	1008
	Had	Tungsten	Liquid-Argon		754
	Total				179166

Table 3.2: Summary of the sampling calorimeters in the calorimetry section, their coverage in η, and the 179166 readout channels. Here, "EM" means the calorimeter component measures an electromagnetic shower, while "Had" means the calorimeter component measures a hadronic shower.

To wrap up this section, I want to briefly discuss an important characteristic of calorimeters: energy resolution. A natural feature that comes out of the calorimeter is the improved energy resolution as the energy increases[18]. Luckily, the upgrades at the LHC mean that even more highly-energetic particles will be measured by the calorimeters and that comes with improved resolution at no cost[19]. In most cases, the calorimeter energy resolution improves with energy as $1/\sqrt{E}$, where E is the energy of the incident particle. For practical purposes, the resolution is reported [23] as a number with 3 components as in eq. (3.8)

$$\frac{\sigma(E)}{E} = \frac{a}{\sqrt{E}} \oplus \frac{b}{E} \oplus c, \tag{3.8}$$

[18]Another feature is that the electromagnetic showers grow in size as well, which is why deeper calorimeters are needed at higher energies

[19]There are downsides such as much harder radiation impacting the instrumentation means more repairs, maintenance, and upgrades.

where the symbol '$\oplus$' indicates a quadratic sum. The first term a represents the "stochastic term", the second term b represents the "noise term", and the third term represents the "constant term". Each of these terms is understood by their dependency on the energy of the incident particle E. The "stochastic" term arises out of the calorimeter response being proportional to the number of track segments in the shower and a statistical argument can be made to show that this depends on $\sqrt{E}$. This is usually the dominant term that limits the resolution of a calorimeter at low energies. The "noise" represents the electronic noise in the readout chain. The "constant" term includes contributions that do not depend on the energy of the particle such as how the calorimeter shapes the the particle impact point or nonuniformity of the detector geometry. At high energies, calorimeter resolution is limited by the "constant" term. For ATLAS, the quoted energy resolution [24, Chapter 33. Particle detectors] for the EMCal is

$$\frac{\sigma(E)}{E} = \frac{10\%}{\sqrt{E}} \oplus \frac{0.3}{E} \oplus 0.4\% \tag{3.9}$$

To interpret this correctly, a 100 GeV electron will have $\frac{\sigma(E)}{E} = 1\% \oplus 0.003 \oplus 0.4\% = 1.1\%$ while a 10 GeV electron will have $\frac{\sigma(E)}{E} = 40\%$. At this low energy, the tracking section 3.6 will help improve this measurement from the calorimeter. In [25], ATLAS measured the jet energy resolution in Run 1 to be from 20% to 10% for jets within $|y| < 2.8$[20] and $30\,\text{GeV} < p_{\text{T}} < 500\,\text{GeV}$.

3.8 Muons and the Muon Spectrometer

The conceptual layout of the muon spectrometer (MS) is shown in fig. 3.17. This entire system [3, 26] is based on the magnetic deflection of muon tracks in the large superconducting toroid magnets. For $|\eta| < 1.4$, the magnetic bending is provided by the large barrel toroid;

[20]Rapidity.

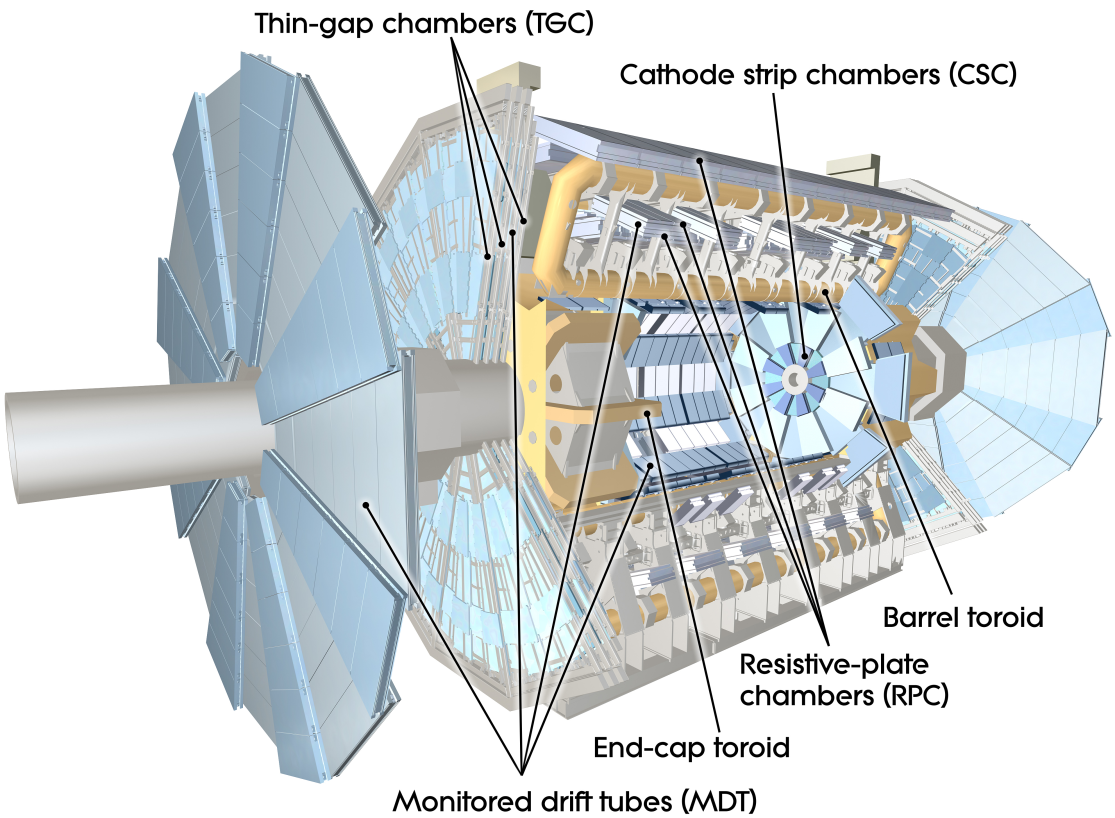

Figure 3.17: [3] A cut-away view of the ATLAS muon system.

for $1.6 < |\eta| < 2.7$, the muon tracks are bent by two smaller end-cap magnets inserted into both ends of the barrel toroid; and in the transition region $1.4 < |\eta| < 1.6$ the bending is provided by both the end-cap and barrel fields. In the barrel (transition and end-cap) region, the muon tracks are measured in chambers arranged in three cylindrical (planes) layers parallel (perpendicular) to the beam axis. The coverage and number of channels is summarized in table 3.3.

The Monitored Drift Tubes (MDT) [27] (1163 chambers) and Cathode Strip Chambers (CSC) [28] (32 chambers) provide the precision measurements for the system. Over most of the η range, this is largely done by MDT, while CSC takes over for large pseudorapidities. For $\eta < 2.4$ the trigger chambers has the unique role of providing bunch-crossing identification, well-defined p_{T} trigger thresholds, and measure the muon coordinate in a direction orthogonal to the precision-tracking chambers. The trigger chambers is composed of Resistive Plate Chambers (RPC) [29] and Thin Gap Chambers (TGC) [30].

Detector	Coverage	Channels	Number of
MDT	$\|\eta\| < 2.0$	354000	
CSC	$2.0 < \|\eta\| < 2.7$	31000	
RPC	$\|\eta\| < 1.05$	373000	
TGC	$1.05 < \|\eta\| < 2.4$	318000	

Table 3.3: Summary of the components of the muon spectrometer, their coverage in η, and the number of readout channels.

Glossary

ATLAS a general-purpose detector at the LHC. 1, 11, 13, 25

CERN European Organization for Nuclear Research. 1

CSC Cathode Strip Chambers. 27, 28

EMB LAr electromagnetic barrel. 21, 23, 24

EMCal electromagnetic calorimeter. 23, 25

EMEC LAr Elecromagnetic End-Cap Calorimeter. 21, 23, 24

FCal forward calorimeter. 23, 24

HEC LAr Hadronic End-Cap Calorimeter. 23, 24

HL-LHC High Luminosity LHC. 4

ID Inner Detector. 11, 15–18

LAr Liquid Argon Calorimeter. 21–24

LHC Large Hadron Collider. 1, 2, 8, 13, 24

MDT Monitored Drift Tubes. 27, 28

MS muon spectrometer. 27

PS Proton Synchotron. 3

PSB Proton Synchotron Booster. 3

punch-through For jets at very high transverse momentum it is possible that part of the energy is not deposited in the calorimeter, but leaks out to the detector components beyond the calorimeter. This leads to a systematic reduction in the measured jet energy. Jets that deposit energy beyond the hadronic Tile calorimeter and in the muon system are called punch-through jets. [31]. 21

RPC Resistive Plate Chambers. 27, 28

SCT Semiconductor Tracker. 16–18

SPS Super Proton Synchotron. 3, 13

TGC Thin Gap Chambers. 27, 28

Tile Tile calorimeter. 23, 24

TRT Transition Radiation Tracker. 16–19

Bibliography

[1] Lyndon Evans and Philip Bryant. "LHC Machine". In: *JINST* 3.08 (2008), S08001. DOI: 10.1088/1748-0221/3/08/S08001. URL: http://stacks.iop.org/1748-0221/3/i=08/a=S08001 (cit. on pp. 1, 3, 5, 7, 8).

[2] CERN Service graphique. "Overall view of the LHC. Vue d'ensemble du LHC". In: (June 2014). General Photo. URL: https://cds.cern.ch/record/1708849 (cit. on p. 2).

[3] ATLAS Collaboration. "The ATLAS Experiment at the CERN Large Hadron Collider". In: *JINST* 3 (2008), S08003. DOI: 10.1088/1748-0221/3/08/S08003 (cit. on pp. 1, 10, 12, 16, 17, 19, 20, 22, 24, 26, 27).

[4] The CMS Collaboration. "The CMS experiment at the CERN LHC". In: *Journal of Instrumentation* 3.08 (2008), S08004. DOI: 10.1088/1748-0221/3/08/S08004. URL: http://stacks.iop.org/1748-0221/3/i=08/a=S08004 (cit. on p. 1).

[5] The LHCb Collaboration. "The LHCb Detector at the LHC". In: *Journal of Instrumentation* 3.08 (2008), S08005. DOI: 10.1088/1748-0221/3/08/S08005. URL: http://stacks.iop.org/1748-0221/3/i=08/a=S08005 (cit. on p. 1).

[6] The ALICE Collaboration. "The ALICE experiment at the CERN LHC". In: *Journal of Instrumentation* 3.08 (2008), S08002. DOI: 10.1088/1748-0221/3/08/S08002. URL: http://stacks.iop.org/1748-0221/3/i=08/a=S08002 (cit. on p. 1).

[7] L Rossi. "The LHC superconducting magnets". In: *Particle Accelerator Conference, 2003. PAC 2003. Proceedings of the*. Vol. 1. IEEE. 2003, pp. 141–145 (cit. on pp. 1, 2).

[8] Esma Mobs. "The CERN accelerator complex." In: (July 2016). General Photo. URL: https://cds.cern.ch/record/2197559 (cit. on p. 3).

[9] *HL-LHC High Luminosity Large Hadron Collider: The HL-LHC project*. http://hilumilhc.web.cern.ch/about/hl-lhc-project (cit. on p. 4).

[10] ATLAS Collaboration. *ATLAS Luminosity Public Results Run 2*. https://twiki.cern.ch/twiki/bin/view/AtlasPublic/LuminosityPublicResultsRun2. [Online; accessed 11-March-2018]. 2015 (cit. on pp. 5, 6, 9).

[11] ATLAS Collaboration. "Luminosity determination in pp collisions at $\sqrt{s} = 8$ TeV using the ATLAS detector at the LHC". In: *Eur. Phys. J. C* 76 (2016), p. 653. DOI: 10.1140/epjc/s10052-016-4466-1. arXiv: 1608.03953 [hep-ex] (cit. on p. 5).

[12] J. Barranco García et al. "Long term dynamics of the high luminosity Large Hadron Collider with crab cavities". In: *Phys. Rev. Accel. Beams* 19 (10 Oct. 2016), p. 101003. DOI: 10.1103/PhysRevAccelBeams.19.101003. URL: https://link.aps.org/doi/10.1103/PhysRevAccelBeams.19.101003 (cit. on p. 7).

[13] *ATLAS inner detector: Technical Design Report, 1*. Technical Design Report ATLAS. Geneva: CERN, 1997. URL: http://cds.cern.ch/record/331063 (cit. on p. 15).

[14] S Haywood et al. *ATLAS inner detector: Technical Design Report, 2*. Technical Design Report ATLAS. Geneva: CERN, 1997. URL: https://cds.cern.ch/record/331064 (cit. on p. 15).

[15] Norbert Wermes and G Hallewel. *ATLAS pixel detector: Technical Design Report*. Technical Design Report ATLAS. Geneva: CERN, 1998. URL: http://cds.cern.ch/record/381263 (cit. on p. 17).

[16] W. R. Bennett. "Spectra of quantized signals". In: *The Bell System Technical Journal* 27.3 (July 1948), pp. 446–472. ISSN: 0005-8580. DOI: 10.1002/j.1538-7305.1948.tb01340.x (cit. on p. 17).

[17] ATLAS Collaboration. "The silicon microstrip sensors of the ATLAS semiconductor tracker". In: *Nuclear Instruments and Methods in Physics Research Section A: Accelerators, Spectrometers, Detectors and Associated Equipment* 578.1 (2007), pp. 98–118. ISSN: 0168-9002. DOI: https://doi.org/10.1016/j.nima.2007.04.157. URL: http://www.sciencedirect.com/science/article/pii/S0168900207007644 (cit. on p. 18).

[18] The ATLAS TRT collaboration. "The ATLAS Transition Radiation Tracker (TRT) proportional drift tube: design and performance". In: *Journal of Instrumentation* 3.02 (2008), P02013. URL: http://stacks.iop.org/1748-0221/3/i=02/a=P02013 (cit. on p. 18).

[19] The ATLAS TRT collaboration. "The ATLAS TRT Barrel Detector". In: *Journal of Instrumentation* 3.02 (2008), P02014. URL: http://stacks.iop.org/1748-0221/3/i=02/a=P02014 (cit. on p. 18).

[20] W. Riegler et al. "Resolution limits of drift tubes". In: *Nuclear Instruments and Methods in Physics Research Section A: Accelerators, Spectrometers, Detectors and Associated Equipment* 443.1 (2000), pp. 156–163. ISSN: 0168-9002. DOI: https://doi.org/10.1016/S0168-9002(99)01014-1. URL: http://www.sciencedirect.com/science/article/pii/S0168900299010141 (cit. on p. 18).

[21] *ATLAS liquid-argon calorimeter: Technical Design Report*. Technical Design Report ATLAS. Geneva: CERN, 1996. URL: https://cds.cern.ch/record/331061 (cit. on p. 21).

[22] *ATLAS tile calorimeter: Technical Design Report*. Technical Design Report ATLAS. Geneva: CERN, 1996. URL: https://cds.cern.ch/record/331062 (cit. on p. 21).

[23] Christian Wolfgang Fabjan and F Gianotti. “Calorimetry for Particle Physics”. In: *Rev. Mod. Phys.* 75.CERN-EP-2003-075 (Oct. 2003), 1243–1286. 96 p. URL: https://cds.cern.ch/record/692252 (cit. on pp. 23, 25).

[24] C. Patrignani et al. “Review of Particle Physics”. In: *Chin. Phys.* C40.10 (2016), p. 100001. DOI: 10.1088/1674-1137/40/10/100001 (cit. on p. 26).

[25] ATLAS Collaboration. “Jet energy resolution in proton–proton collisions at $\sqrt{s} = 7$ TeV recorded in 2010 with the ATLAS detector”. In: *Eur. Phys. J. C* 73 (2013), p. 2306. DOI: 10.1140/epjc/s10052-013-2306-0. arXiv: 1210.6210 [hep-ex] (cit. on p. 26).

[26] *ATLAS muon spectrometer: Technical Design Report*. Technical Design Report ATLAS. Geneva: CERN, 1997. URL: https://cds.cern.ch/record/331068 (cit. on p. 26).

[27] F. Bauer et al. “Construction and test of MDT chambers for the ATLAS muon spectrometer”. In: *Nuclear Instruments and Methods in Physics Research Section A: Accelerators, Spectrometers, Detectors and Associated Equipment* 461.1 (2001). 8th Pisa Meeting on Advanced Detectors, pp. 17–20. ISSN: 0168-9002. DOI: https://doi.org/10.1016/S0168-9002(00)01156-6. URL: http://www.sciencedirect.com/science/article/pii/S0168900200011566 (cit. on p. 28).

[28] T. Argyropoulos et al. “Cathode strip chambers in ATLAS : Installation, commissioning and in situ performance”. In: *2008 IEEE Nuclear Science Symposium Conference Record*. Oct. 2008, pp. 2819–2824. DOI: 10.1109/NSSMIC.2008.4774958 (cit. on p. 28).

[29] G. Aielli et al. “The RPC first level muon trigger in the barrel of the ATLAS experiment”. In: *Nuclear Physics B - Proceedings Supplements* 158 (2006). Proceedings of the 8th International Workshop on Resistive Plate Chambers and Related Detectors, pp. 11–15. ISSN: 0920-5632. DOI: https://doi.org/10.1016/j.nuclphysbps.

2006.07.031. URL: http://www.sciencedirect.com/science/article/pii/S0920563206004178 (cit. on p. 28).

[30] S. Majewski et al. “A THIN MULTIWIRE CHAMBER OPERATING IN THE HIGH MULTIPLICATION MODE”. In: *Nucl. Instrum. Meth.* 217 (1983), pp. 265–271. DOI: 10.1016/0167-5087(83)90146-1 (cit. on p. 28).

[31] ATLAS Collaboration. “Jet energy measurement with the ATLAS detector in proton–proton collisions at $\sqrt{s} = 7$ TeV”. In: *Eur. Phys. J. C* 73 (2013), p. 2304. DOI: 10.1140/epjc/s10052-013-2304-2. arXiv: 1112.6426 [hep-ex] (cit. on p. 30).